High-flux bright x-ray source from femtosecond laser-irradiated microtapes

Check for updates

Xiaofei Shen [1], Alexander Pukhov [1] ✉ & Bin Qiao [2] ✉

Betatron x-ray sources from laser-plasma interaction are characterized by compactness, ultrashort duration, broadband spectrum and micron source size. However, high-quality measurements with good statistics, especially in a single shot, require fluxes and energies beyond the current capabilities. Here, we propose a method to enhance the flux and brightness of the betatron sources without increasing the laser energy. By irradiating an edge of a microtape target with a femtosecond laser, a strong surface plasma wave (SPW) is excited at the edge and travels along the lateral plasma-vacuum interfaces. Tens of nC of electrons are peeled off and accelerated to superponderomotive energies by the longitudinal field of the SPW, whilst undergoing transverse betatron oscillations, leading to emission of hard x-rays. Via three-dimensional particle-in-cell simulations, we demonstrate that a tabletop 100 TW class femtosecond laser can produce an ultrabright hard x-ray pulse with flux up to 10^7 photons eV^{-1} and brilliance about 10^{23} photons s^{-1} mm^{-2} $mrad^{-2}$ $0.1\%BW^{-1}$, paving the way for single-shot x-ray measurements in ultrafast science and high-energy-density physics.

Ever since its discovery in 1895 by Röntgen, x-ray radiation has always been pushing the frontiers of our knowledge as one of the most powerful tools for exploring the properties of matter[1–3]. State-of-the-art x-ray sources can produce ultrabright x-rays at keV photon energies[4–8]. They have become indispensable for many applications in fundamental research, industry and medicine. However, despite the extensive demand, only a few dedicated synchrotrons and x-ray free-electron lasers exist in the world, because limited by the weak acceleration field of radio-frequency accelerators, these facilities are usually very large and expensive. Furthermore, the natural narrowband spectrum from undulators imposes restrictions on their applications in several important diagnostics for material science and high-energy-density (HED) physics[9].

In relativistic laser plasma-based accelerators, the excited accelerating field strength can be several orders of magnitude higher, and therefore, laser-plasma based radiation sources have been proposed to be an attractive alternative for modern x-ray applications. In the last two decades, x-ray sources based on laser wakefield accelerators (LWFA) have been widely investigated[10–25]. However, in LWFA, the accelerated electron beam is characterized by moderate charge (about hundreds of picocoulombs to nanocoulombs)[26,27], which determines that the conversion efficiency of laser energy to photons and the photon number are relatively low. The total number of photons in full spectrum is usually on the order of 10^8, and the peak flux is about 10^4–10^5 photons $eV^{-13,28}$. This is not sufficient to make high-quality measurements, especially in a single-shot. For instance, to achieve good statistics, x-ray absorption spectroscopy techniques, as essential tools for probing both electronic and atomic structural properties of matter, require the flux satisfying $N_{ph} > 10^6$ $eV^{-13,29–32}$, where N_{ph} is the number of photons in the energy band of interest. This is simply determined by the requirement that the random statistic noise $SN = 1/\sqrt{N_{ph}}$ should be smaller than 1/1000 of the signal, while recent experiments indicate that due to background noise, an even higher flux about 10^7 photons eV^{-1} is necessary to fulfill the required signal-to-noise ratio[33]. On the other hand, for many applications, especially in HED experiments[3,33–38], single-shot measurements are crucial because of complex target designs and low repetition rate of powerful lasers. Though it is possible to make such measurements by utilizing implosion-based x-ray sources[39–41], they are based on large, expansive and unique facilities and their brilliance is relatively low[3]. Therefore, it is critical to develop tabletop ultrabright high-flux x-ray sources.

Recently, there has been a growing focus on enhancing the photon flux of x-rays at keV range. Most of the works are based on delicate manipulation of the LWFA by making a trade-off between high brilliance and high flux[33,42–47] due to the limitation of the beam loading effect[48]. Another approach to achieving higher flux involves using electrons from direct laser acceleration (DLA) mechanism with near-critical-density plasmas[49–53] or microwires[54,55], where compared to the LWFA, much larger number of electrons but with lower energy and larger angular spread are produced. The divergence of the emitted x-rays is usually around hundreds of mrad,

[1]Institut für Theoretische Physik I, Heinrich-Heine-Universität Düsseldorf, 40225 Düsseldorf, Germany. [2]Center for Applied Physics and Technology, HEDPS, SKLNP, and School of Physics, Peking University, Beijing 100871, China. ✉e-mail: pukhov@tp1.uni-duesseldorf.de; bqiao@pku.edu.cn

leading to rather low brilliance[56–61]. Moreover, electron acceleration and coherent harmonics generation in laser-microtape target interaction at oblique incidence[62–64] and MeV electron acceleration driven by THz surface waves in laser-microwire interaction[65] have been investigated. Until now, in spite of the significant demand in diverse applications, how to achieve ultrabright femtosecond x-rays with a flux of up to or even beyond 10^7 photons eV^{-1} at keV range still remains an open question.

In this paper, we demonstrate a scheme for generation of high-flux high-brilliance x-ray radiations, where a linearly-polarized (LP) femtosecond laser pulse is incident on an edge of a submillimeter wide microtape, as illustrated in Fig. 1a. When the laser pulse impinges on the edge, a strong surface plasma wave (SPW) is easily excited and significant amounts of electrons are peeled off from the tape into vacuum. These electrons will be accelerated forward to superponderomotive energies, while undergoing betatron oscillations near the lateral plasma-vacuum interfaces, leading to intense x-ray bursts. Our three-dimensional (3D) particle-in-cell (PIC) simulations demonstrate that by utilizing a readily available tabletop 150 TW femtosecond laser, hard x-ray sources characterized by flux up to 10^7 photons eV^{-1} around 5 keV and peak brilliance about 10^{23} photons s^{-1} mm^{-2} $mrad^{-2}$ $0.1\%BW^{-1}$ can be generated. The energy conversion efficiency is about 2.5×10^{-4}. We have identified the existence of the SPW and demonstrated that the radiating electrons are primarily accelerated by the longitudinal electric field of the SPW and undergo betatron oscillations in the self-generated quasistatic transverse electric and magnetic fields at the vicinity of the interfaces. Our theoretical model fits well with the numerical results.

Results
Source characterization
Figure 1 illustrates the 3D simulation results. When the laser pulse impinges on the front edge of the relativistically overdense plasmas (gray cuboid), a strong SPW can be easily induced without requiring special resonance condition[66]. It propagates along the plasma-vacuum interfaces with a velocity close to the light speed c[67–70]. Subsequently, electrons are continuously peeled off by the transverse field E_y [Fig. 1b] and accelerated forward by the self-generated longitudinal field E_x [Fig. 2c], forming periodically distributed electron nanobunches on both sides of the target [Fig. 1a]. The maximum electron γ already reaches about 400 at $t = 40T_0$, and most of high-energy electrons are confined close to the lateral interfaces.

The angular distribution of electrons is shown in Fig. 1c. The divergence angle is about 5° which is much smaller than that observed in DLA[49,53,57]. The effective electron temperature reaches about 25 MeV, about four times higher than the ponderomotive scaling of 6.7 MeV[71]. There are about 3.1×10^{11} high-energy electrons (~ 50 nC) with $\gamma > 10$ generated along the moving window. This is more than one order of magnitude higher than the typical LWFA results[26,27]. Such high charge, superponderomotive, collimated electrons produce ultrabright radiations near the lateral surfaces since there they experience transverse betatron oscillations in strong self-generated fields.

The obtained photon energy spectrum at $t = 120T_0$ is shown in Fig. 1e. The peak brightness is up to about 4.5×10^7 photons $0.1\%BW^{-1}$ with critical energy of 20 keV. The number of photons with energy > 10 keV (i.e., hard x-ray) reaches 8.6×10^{10}. The x-ray flux is high up to 10^7 photons eV^{-1} around 5 keV region and the corresponding spectral yield efficiency is about 2.2×10^6 photons eV^{-1} J^{-1}. Both are more than one order of magnitude higher than the LWFA results at the laser energy[3,28,33]. This is the key advantage of our scheme compared to other known regimes. Such a high photon flux is crucial for achieving single-shot high-quality measurements[3,33]. The total radiated energy is about 1.1 mJ, resulting in a laser-to-photon conversion efficiency of 2.5×10^{-4}, about one order of magnitude higher than that in other betatron schemes[56,58,72]. Though comparable conversion efficiency was observed in the interaction of PW fs lasers with near-critical-density plasmas[73], in our scheme, the obtained
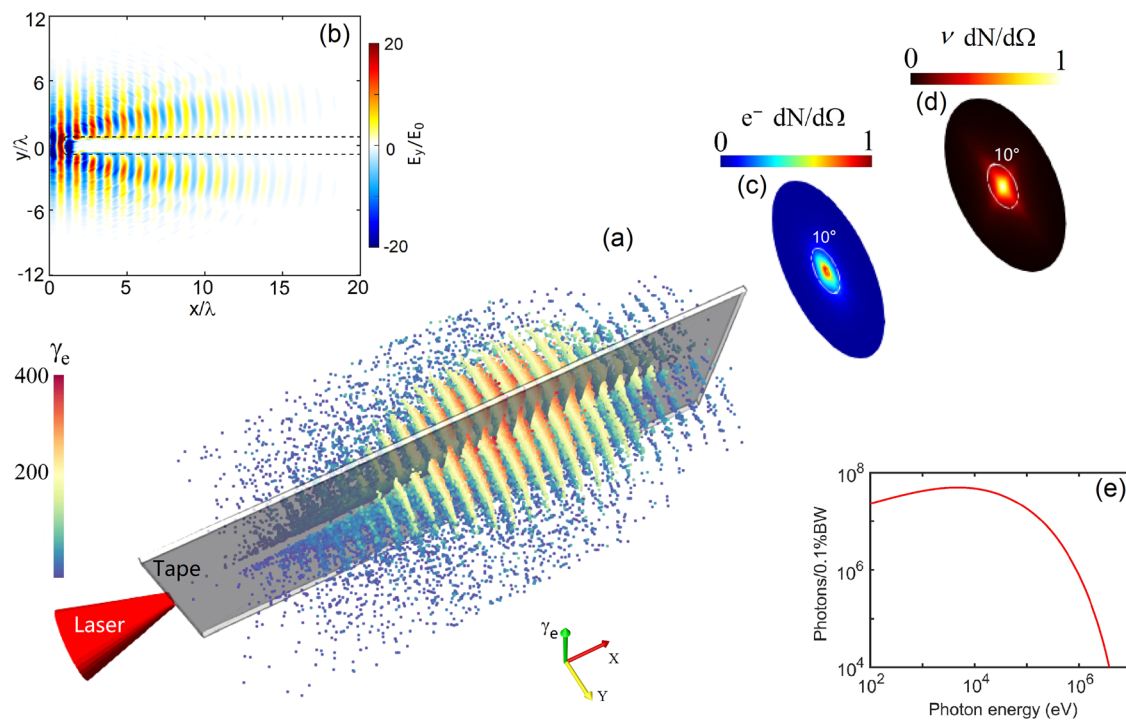

Fig. 1 | Schematic and three-dimensional particle-in-cell simulation results. a An intense femtosecond laser pulse (red cone) is incident on an edge of a submillimeter wide microtape target (gray cuboid) to drive electron acceleration and betatron radiation. Distribution of energetic electrons at $t = 40T_0$ is represented by the spheres where each individual electron is color-coded with its γ-factor. Note that the tape target can be infinitely long along z-direction and our scheme can tolerate the existence of a short-scale preplasma. **b** Transverse field E_y at $t = 0$ when the peak laser enters the simulation box. **c, d** Angular distributions of the electrons and photons, respectively. **e** Final photon spectrum at $t = 120T_0$. Here $d\Omega = \sin\theta d\theta d\phi$ with $\theta = \arctan(\sqrt{p_y^2 + p_z^2})/p_x$ and $\phi = \arctan(p_z/p_y)$, $T_0 = 2\pi/\omega_L$ and the field is normalized to $E_0 = m_e c \omega_L/e$.
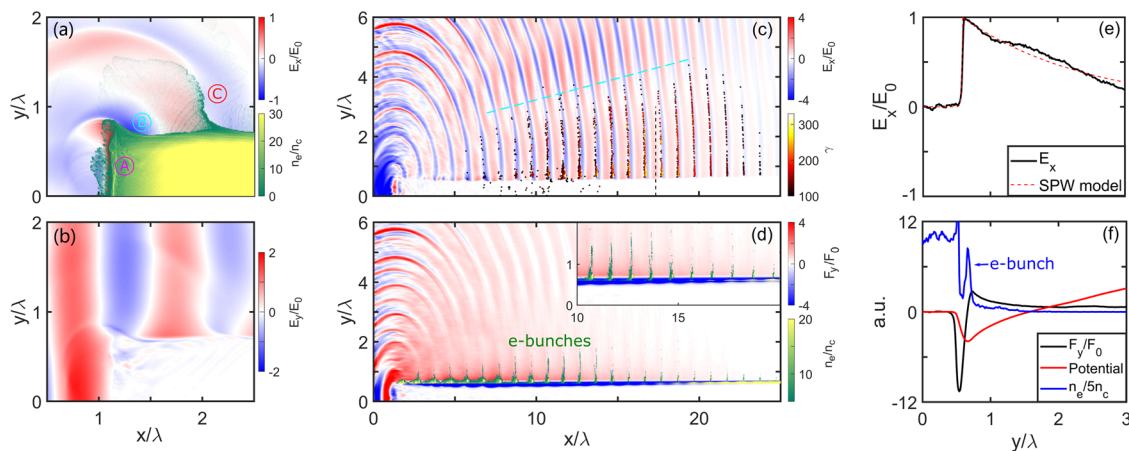
Fig. 2 | Identification of the electron injection, acceleration and betatron oscillation processes. a Electron density (green-yellow) and longitudinal field E_x (blue-red) at $t = -16T_0$, in which `A', `B' and `C' mark three different electron nanobunches in space, but can also be used to phenomenologically represent the compression, injection and acceleration stages of the same electron bunch over time. **b** Transverse field E_y at $t = -16T_0$. **c** Longitudinal field E_x at $t = 12.5T_0$ and electron phase space (black-yellow dots), while (**d**) shows the transverse field F_y and the electron density distribution (green-yellow), where the electron density below $y < 0.6\lambda$ and $n_e < 5n_c$ are removed to clearly show the F_y. The inset is a zoom-in. In (**c**), the dashed cyan line demarcates the surface plasma wave (SPW)-dominated region (below) from the diffracted wave-dominated (above). **e** Comparison of the transverse profile of the SPW model (red dashed) and E_x (black) from the PIC simulation, extracted from the vertical black dashed line marked in (**c**). **f** The 1D profiles of n_e (blue), F_y (black) and the potential (red) obtained from (**d**).

critical energy and hard x-ray photon flux are much higher and divergence is significantly lower.

Figure 1d presents the angular distribution of photons. The opening angles θ_y and θ_z (RMS) are about 50 mrad and 60 mrad, respectively. The source size $d_y \times d_z \approx 5\,\mu m^2$, where d_y [estimated as the sum of l_y and averaged transverse oscillation amplitudes, see Fig. 3e] and d_z ($\sim d_L$) are diameters along y- and z-direction, respectively. Taking the x-ray pulse duration as 30 fs ($\sim \tau_L$), we have the peak brilliance about 10^{23} photons s^{-1} mm^{-2} mrad^{-2} 0.1%BW^{-1}. This is comparable to state-of-the-art third-generation synchrotrons. We highlight that in diagnostic applications, though the x-ray divergence is relatively larger than that obtained in the LWFA regimes[33], it is feasible to ensure that the sample collects the entire photon beam by simply adjusting the source to sample (and sample to detector) distance.

Electron acceleration

To reveal the underlying physics, 2D simulations with particle tracer are performed. The laser and plasma parameters remain the same as described above.

When the laser pulse hits the front edge of an overdense tape target, not only is it cut into two parts [Fig. 1b], but also piles up electrons into a compressed overdense layer in front of the target. A strong SPW can be effectively excited since both the laser pulse and the SPW propagate along the target lateral surfaces at velocities close to the light speed c. The resonance conditions of $\omega_L = \omega_{SP}$ and $k_L = k_{SP}$ can be easily satisfied[67–69], where ω_L and k_L are the laser frequency and wavenumber, respectively, while ω_{SP} and k_{SP} corresponding to the frequency and wavenumber of the SPW. After fast Fourier transformation, in (ω, k) space, by considering a target with a lower electron density of $n_e = 5n_c$ to make the dispersion relations of the laser pulse and SPW discernible, we identified the existence of the SPW at the flat interface, see Supplementary Note I and Fig. S2.

Considering that the physics and phenomena are similar in both sides of the target except for a phase shift [see Fig. 1a, b], in Fig. 2, we elucidate the key physics by only showcasing the results above the target (i.e., $y > 0$). For a LP laser pulse, its Lorentz force has an oscillating component, and therefore, this dense layer will be dragged back at later time [marked as electron nanobunch 'A' in Fig. 2a]. If at the same time the local laser field E_y [Fig. 2b] is negative, the layer will be deflected upward whilst moving backward, forming the electron nanobunch 'B'. Electrons located in the region of a negative longitudinal field E_x will be

further injected into the accelerating phase and accelerated to high energies. This forms the accelerated electron nanobunches above the tape target, corresponding to the bunch 'C' in Fig. 2a and those displayed in Figs. 1a and 2d. In contrast, those experiencing a positive E_x field will be decelerated and debunched to very low density. On the other hand, if the backward electrons feel a positive E_y field, the dense layer will be turned downward, but part of them can also be injected and accelerated to high energies, forming the electron nanobunches below the target [see Fig. 1a].

Figure 2c illustrates the distribution of the E_x field (blue-red) and the phase space of electrons (black-yellow dots) at $t = 12.5T_0$, where to show it clearly, only electrons with $\gamma > 100$ are shown. It is evident that most high-energy electrons are located in the negative components of the E_x field and the majority of them including those most energetic ones are confined very close to the plasma-vacuum interface [see Fig. 2d]. Since the phase velocity of the SPW $v_{ph}^{SPW} = \omega/k_x \approx c(1 - \omega^2/\omega_{pe}^2)$ is very close to the light speed c, electrons can stay in the accelerating phase for tens of laser periods and be accelerated to hundreds of MeV[68].

Figure 3a shows the energy-gain plane (Γ_x, Γ_y) of every electron, while in Fig. 3b, the red and blue lines depict energy spectra of electrons from longitudinal field dominant acceleration (LFDA, $\Gamma_x > \Gamma_y$) and transverse field dominant acceleration (TFDA, $\Gamma_x < \Gamma_y$), respectively. Here $\Gamma_x = -\int ev_x E_x dt$ and $\Gamma_y = -\int ev_y E_y dt$ represent the accumulated work from the longitudinal and transverse fields, respectively. One can clearly see that most energetic electrons are predominantly accelerated by the longitudinal field and the number of LFDA electrons is much higher that of TFDA ones.

To further understand which group of electrons is responsible for the x-ray generation, in Fig. 3e, we show trajectories of some representative electrons from the LFDA. While they are accelerated forward, each of them undergoes multiple betatron oscillations near the lateral plasma-vacuum interface, where both the longitudinal accelerating and transverse wiggling fields are the strongest. Therefore, at each turning point, these electrons emit x-rays efficiently. Their oscillation strength which can be estimated as the amplitude of p_y is $K \approx 10$ [see Fig. 3d], indicating the radiations occur in the wiggler regime[2], in which the opening angle of the radiation cone is much smaller than the maximum angle between the electron velocity and the propagation. In comparison, the TFDA electrons almost move straightly, except at the turning points, but most of them are only reflected once and then never come back, see Supplementary Note V and Fig. S6. Considering that the number and energy of the TFDA electrons are both relatively small,
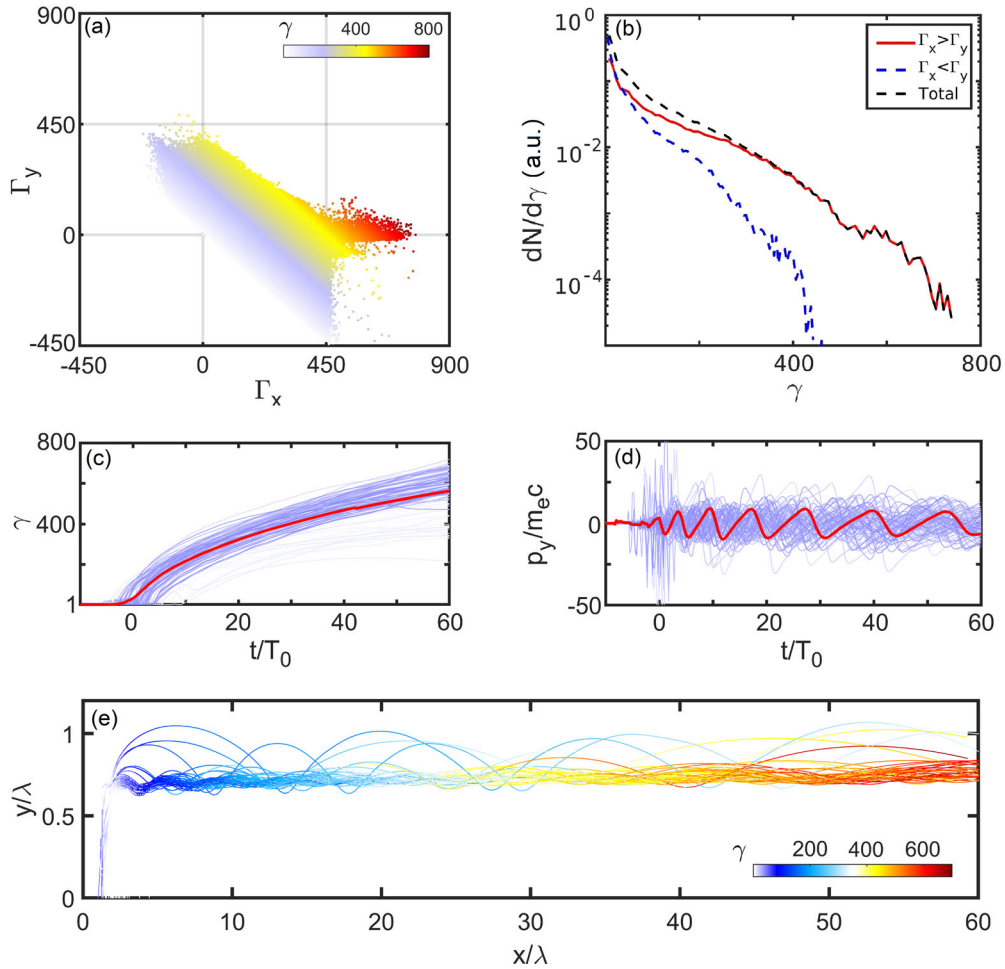
Fig. 3 | Energy spectra and typical trajectories of electrons. a Energy-gain plane (Γ_x, Γ_y) of electrons with their net γ-factor color coded. **b** Electron energy spectra, where the black, red and blue lines represent the energy spectra of the total electrons, the longitudinal field dominant acceleration (LFDA) and transverse field dominant acceleration (TFDA) electrons, respectively. **c, d** Temporal evolution of the γ-factor and p_y of the tracked LFDA electrons, respectively, demonstrating that the γ-factors of the electrons are continuously increasing while undergoing transverse betatron oscillations, highlighted with the red lines from a single electron. **e** Trajectories of representative electrons from the LFDA mechanisms, respectively. In (**c, d**), representative electrons from both sides of the plasma are included.

their contributions to radiation are negligible. Hence, the transverse oscillating LFDA electrons are the main interest here.

In Fig. 3(c) and (d), we correspondingly show the temporal evolution of the γ and p_y of the representative electrons from the LFDA group. One can see that the values of the γ is continuously increasing even when p_y changes sign. This indicates that the electron acceleration and the recoil force of electron betatron motion cannot directly stem from the laser fields. Otherwise, the γ should be oscillating when p_y changes sign[49]. Therefore, we further identify the origin of the acceleration and wiggling fields. This is essential for optimizing the electron acceleration and betatron radiation.

In laser-plasma interactions, different modes can be excited especially in our scheme, including the SPW aforementioned, the diffracted wave, the high-order harmonics etc. As shown in Fig. 2(a), near the target edge, the profile of the E_x field is curved which indicates that it is combined by both the SPW and the diffracted wave. However, the diffracted wave diverges to all the directions in the propagation, leading to a rapid decrease of its amplitude. In contrast, the SPW mainly travels forward along the plasma-vacuum interface and its amplitude decreases very slowly. Figure 2(c) displays the distribution of the E_x field at $t = 12.5T_0$, where one can clearly see a gap (highlighted with a cyan dashed line) which roughly demarcates the SPW-dominated region (below) from the diffracted wave-dominated region (above). In other words, the E_x field near the interface is mainly contributed by the longitudinal component of the SPW.

To further demonstrate the E_x field responsible for the acceleration of the radiating electrons (i.e., the LFDA electrons) indeed stemming from the SPW, we compared the transverse profile of the E_x field to the prediction of the SPW theory. By considering an SPW propagating along the interface between vacuum and a cold plasma and assuming the field having the form[67,69]

$$E_{sw} = E_{sw0}e^{-k_y y}e^{-i(\omega t - k_x x)} \tag{1}$$

where E_{sw0} is the field amplitude. For the field on the vacuum side,

$$k_{xv} = \frac{\omega}{c}\sqrt{\frac{1 - n_e/n_c}{2 - n_e/n_c}}, \quad k_{yv} = \frac{\omega}{c}\sqrt{\frac{1}{n_e/n_c - 2}}. \tag{2}$$

For overdense plasmas with $n_e/n_c \gg 2$, $k_{yv} > 0$, which means the SPW decays in y-direction, but very slowly. The characterize length for the field decaying to $1/e_N$ is $\lambda\sqrt{n_e/n_c - 2}/2\pi > \lambda$ which is much longer than the amplitude of the betatron oscillations shown in Fig. 3e. Here $e_N = 2.71828...$ is the Euler's number. For the field on the plasma side,

$$k_{xp} = k_{xv}, \quad k_{yp} = \frac{\omega}{c}\left(\frac{n_e}{n_c} - 1\right)\sqrt{\frac{1}{n_e/n_c - 2}}. \tag{3}$$

Therefore, inside the plasma the SPW fields decay much faster.

In order to compare with the above theory, we extracted the transverse profile of the E_x field at $x = 17.35\lambda$ as marked by the vertical black dashed line in Fig. 2c. Its profile is depicted by the black solid line in Fig. 2e, while the prediction of the SPW model according to Eqs. (1), (2) and (3) is presented by the red dashed line. One can clearly see that the simulation result fits quite well with the SPW model and the E_x field decreases slowly along y-direction. Here n_e and E_{sw0} are determined from the simulation and we choose the part with positive E_x field to avoid the effects induced by the electron nano-bunches located in the region of negative components.

Furthermore, to exclude the effects caused by charge-separation field, we also conducted a hybrid 2D simulation with the hybrid VLPL code[74] where the target acts as a metal. The separation between the diffracted fields and the SPW is even more clear. The distribution of the E_x field near the interface fits almost perfectly with the SPW model after a relatively long propagation. Details can be found in the Supplementary Note I and Fig. S1.

The electron density at $t = 12.5T_0$ is shown in Fig. 2d, and the 1D cut is depicted by the blue line in Fig. 2f, where one can see that the density is peaked near the interface. About 92% of electrons outside the initial plasma boundary are confined within $|y| < 3\lambda$. Therefore, in our scheme, it is clear that most of radiating electrons are accelerated by the longitudinal component of the SPW. Only a minor part of them can travel to farther distance along y-direction experiencing TFDA or being accelerated by the diffracted laser field, but their contribution to the x-ray generation is negligible.

Betatron radiation

In order to reveal the source of the recoil force, we present the distribution of the transverse field $F_y = E_y - B_z$ at $t = 12.5T_0$ in Fig. 2d and its 1D cut in Fig. 2f. One can see that F_y is positive above the plasma, but negative inside the skin depth of the plasma. This is because outside the plasma, there is a strong charge-separation field E_y^s between the peeled-off electrons and those almost stationary ions. Thanks to these forward-moving electrons, a return current is formed inside the plasma to maintain the target neutral. This large return current in turn induces a strong localized magnetic field B_z^s that will reflect electrons outward. Its amplitude is much stronger than the charge-separation field, but is constrained in a small region characterized by several skin depths. As a result, the quasistatic attracting E_y^s field and the repelling B_z^s field not only constitute the recoil force that drives the electron betatron motion, but also create a potential well [red line in Fig. 2f] in transverse direction that can confine most electrons at the vicinity of the target lateral surfaces.

So far we have clarified that the radiating electrons are predominantly accelerated by the longitudinal components of the SPW, whilst wiggled by the self-generated transverse fields along the forward propagation. Note that due to the overdense target used here, our wiggling field up to 4.5×10^{13} V/m [see Fig. 2f] is significantly stronger than that of the LWFA[2,10] and DLA[49,56]. This leads to a very short oscillation wavelength λ_u which is about $10\,\mu m$. Considering that in the wiggler regime, the critical energy $\hbar\omega_c = (3/2)\gamma^3 c/\rho = (3/2)K\gamma^2 hc/\lambda_u$, such a strong wiggling field is the key reason that with $K \approx 10$, we can achieve x-rays with critical energy of tens of keV without requiring GeV-class electrons as in LWFA[3,28]. While the proposed scheme presents some differences in target parameters with respect to the widely investigated LWFA-based betatron x-ray sources, here the electrons still undergo betatron oscillations. Therefore, we retain the name of betatron x-ray source to characterize the fundamental physical process, as in other literature[18,45,58,75].

Theoretical model and scaling

To establish a theoretical model, we consider single electron motion in presence of combined fields of a y-polarized laser pulse (E_y^l, B_z^l) and the self-generated electric $(E_{x,y}^s)$ and magnetic (B_z^s) fields. For simplicity, we exploit 2D (x, y) planar geometry, and use dimensionless variables: $t \rightarrow \omega_L t$, $x \rightarrow k_0 x$, $v \rightarrow v/c$, $p \rightarrow p/m_e c$, $E \rightarrow eE/m_e c\omega_L$. The equations of single electron motion are $d\mathbf{r}/dt = \mathbf{v}$ and $d\mathbf{p}/dt = -(\mathbf{E} + \mathbf{v} \times \mathbf{B})$. Since in the comoving

frame, E_x^s varies very slowly, and therefore can be treated as a constant. As the red line shown in Fig. 2f, we have a skewed potential well. Near the point of the minimum potential energy, the transverse force is assumed to have the form of $F_y^s = E_y^s - v_x B_z^s = \kappa_{i,o} y$, see Supplementary Note II and Fig. S3. Here the subscripts i and o denote inside and outside of the minimum potential energy point. We calculate the coefficients as $\kappa_i = F_{y0}^s k_p$ and $\kappa_o = -k_h^2/e_N$, where $k_{p,h} = \sqrt{n_{p,h}/n_c} k_0$ is the wave number, n_p and n_h represent the local plasma density and the hot electron density, respectively[68,76].

Considering that the longitudinal field dominates the acceleration, and in relativistic limit, $v_x \approx 1 \gg v_y$, we have $E_x^s \gg E_y^l - v_x B_z^l \approx 0$. Then we can write the equation of the electron transverse motion as

$$\frac{d^2 y}{dt^2} + \frac{E_x^s}{\gamma_0 + E_x^s t}\frac{dy}{dt} + \frac{\kappa}{\gamma_0 + E_x^s t} y = 0. \tag{4}$$

This is an equation of a damped oscillator with eigenfrequency $\omega_\beta = \sqrt{\kappa/(\gamma_0 + E_x^s t)}$. On each side of the lowest potential point, the electron orbits can be approximately given as

$$x \simeq x_0 + t, \quad y \simeq y_\beta \cos\left(\frac{2\kappa_{i,o}}{\omega_\beta E_x^s} + \phi\right); \tag{5}$$

$$p_x \approx \gamma_t \simeq \gamma_0 + E_x^s t, \quad p_y \simeq -\gamma_t y_\beta \omega_\beta \sin\left(\frac{2\kappa_{i,o}}{\omega_\beta E_x^s} + \phi\right) \tag{6}$$

where $y_\beta = C_1 \sqrt{\omega_\beta E_x^s/\pi\kappa_{i,o}}$ is the betatron oscillation amplitude, C_1 and ϕ are constants which have to be determined by initial conditions.

According to our simulation results discussed above, we know $F_{y0}^s \simeq 3F_0, n_p \simeq a_0 n_c$ and $n_h \simeq 5n_c$, where $F_0 = m_e c\omega_L$. Then we calculate $|\kappa_i/\kappa_o| \approx 7.3$ and the oscillation period $\tau_i/\tau_o = \sqrt{|\kappa_o/\kappa_i|} \approx 0.4$, which agrees well with the result in Fig. 3d. By taking the electron γ as 500, we have $\tau_o = 2.5\tau_i = 16.5T_0$, leading to the betatron duration of $\tau_\beta = 0.5(\tau_i + \tau_o) \approx 11.5T_0$, which also fits well the simulation results [see Fig. 3d].

From the electron trajectory, we can further study the radiation features by assuming a relativistic electron in instantaneously circular motion with radius ρ. Expressions of the radiated power P_r, the critical frequency ω_c and the radiation angle θ can be written as[2,77]

$$P_r = \frac{2}{3}\gamma^4 \frac{1}{\rho^2}, \quad \omega_c = \frac{3}{2}\gamma^3 \frac{1}{\rho}, \quad \theta = \frac{2\pi y_\beta}{\lambda_\beta}, \tag{7}$$

where $\rho = \lambda_\beta/2\pi\theta$. The total radiated energy can be estimated as $\mathcal{E}_r = N_e P_r L/c$, where N_e is the electron number and L is the acceleration distance. One can estimate the critical energy[10] $\hbar\omega_c = (3/2)\hbar\gamma^2|F_{y0}^s| \approx 17.5$ keV by substituting the electron temperature of $\bar{\gamma} = 50$. Besides, considering the electron initial position is within the skin depth, i.e., $1/k_p$, the amplitude of betatron motion is $y_\beta \simeq 0.062\lambda$, close to the simulation results 0.056λ, shown in Fig. 3e. The opening angle estimated from Eq. (7) gives about 0.066 rad, also in good agreement with the simulation results [Fig. 1d].

In intense laser-solid-density target interactions, the self-generated fields are always mainly determined by the peak laser fields[78-80], which means $E_x^s, E_y^s, B_z^s \propto a_0$, leading to $\gamma_t \propto a_0$. Therefore, $y_\beta \propto (\kappa/\gamma_t)^{1/4} \propto a_0^0$, $\omega_\beta \propto \kappa/E_x^s \propto a_0^0$. Since the energy conversion efficiency to electrons is almost comparable for moderately relativistic laser intensities considered here, $N_e \propto \mathcal{E}_L/T_e \propto a_0$. Finally, we have

$$\omega_c \propto a_0^3, \quad \mathcal{E}_r \propto N_e P_r \propto a_0^5, \quad \theta \propto a_0^0. \tag{8}$$
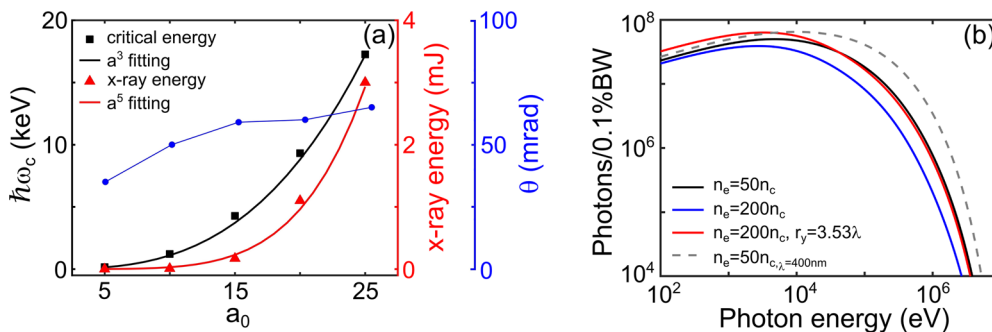
Fig. 4 | Scaling and robustness. a Dependence of synchrotron radiated x-ray energy $\mathcal{E}_r$ (red triangles), critical energy $\hbar\omega_c$ (black squares) and opening angle (blue circles) on a_0. The black and red solid lines correspondingly show fittings of $\mathcal{E}_r$ and $\hbar\omega_c$ according to Eq. (8). Here $\theta = \max\{\theta_y, \theta_z\}$. **b** Final photon spectra from the case with $n_e = 50n_c$ (black), $n_e = 200n_c$ (blue), $n_e = 200n_c$ and an elliptical focal spot with larger $r_y = 3.53\lambda$ (red) and $n_e = 50n_{c,\lambda=400nm}$ (dashed gray). Detailed parameters are introduced in the Discussion section.

To demonstrate these relations, we performed more 3D simulations by varying a_0. The results are shown in Fig. 4a, where the black squares and red triangles represent the simulation results of $\hbar\omega_c$ and $\mathcal{E}_r$, respectively, and the black and red lines show the corresponding fittings from Eq. (8). It is evident that the simulation results are in accordance with the theoretical scalings. Moreover, as predicted by our theory, the radiation divergence is almost independent of a_0, see blue circles in Fig. 4a.

Discussion

The interaction of intense lasers with solid targets has been widely investigated in both theory and experiments[81]. The key difference in the experimental setup between our scheme and previous studies is the incident angle of the laser pulse. Previous studies[81] focused on the schemes where the laser is normally or obliquely incident on a plane of a solid target, while here we demonstrate the physical advantages of the parallel incidence on an edge of a solid target. Compared to these known setups especially those employing normal incidence setups, no special considerations including the ionization of the solid target in the vacuum chamber are required[68]. Note that the ratio of laser energy reflected by the thin edge can be roughly estimated as $d_y/d_L \approx 20\%$, comparable to the 2D simulation result of about 14% though a short-scale preplasma is considered. The potential damage caused by the reflection can be avoided via utilizing a plasma mirror which can also enhance the laser pulse contrast[82,83]. Usually, the reflectivity of plasma mirrors is about 80%[84] and it can be further improved to exceed 90% with a controlled prepulse[85].

Considering that for laser wavelength of 800 nm, the electron density of solid targets is usually above $100n_c$, we did a new simulation with initial electron density of $200n_c$ and the other parameters remaining unchanged to check the effects of the electron density. The obtained photon energy spectrum at $t = 120T_0$ is shown by the blue line in Fig. 4b. The peak flux at 5 keV is about twenty percent lower, but still about 8 times higher than the record reported in the LWFA regime[33]. However, the divergences are even smaller (40 mrad and 30 mrad along y- and z-direction, respectively) benefited from narrower profile of the transverse fields [see detailed discussion in Supplementary Note III and Fig. S4d]. These together actually lead to two times higher brilliance compared to the standard case described in Fig. 1.

Further, to show that our scheme works for metal targets and different wavelength laser pulses, we consider the second-harmonic laser pulses which recently have attracted great interest in experiments due to its high contrast[86–88]. Since the normalized critical density $n_c = m_e\omega_L^2/4\pi e^2$ depends on the wave frequency, for different wavelength laser pulses, the same material is characterized by different normalized densities. For example, for second-harmonic laser pulses, $n_e = 50n_{c,\lambda=400nm}$ already represents the realistic density of plastics and for $n_e = 200n_{c,\lambda=400nm}$, it is even higher than the realistic density of some common metals such as Aluminum and Copper.

We conducted another 3D PIC simulation with $\lambda = 400$ nm and the other normalized parameters remaining the same (i.e., $a_0 = 20$, $d_L = 4.7\lambda$, $n_e = 50n_{c,\lambda=400nm}$) except that the pulse duration is still 30 fs to deliver the same laser energy. The corresponding photon spectrum is shown by the dashed gray line in Fig. 4b. The critical energy is about 37 keV and the flux is about 1.25×10^7 photons eV^{-1} around 5 keV. The opening angles remain almost the same as that shown in Fig. 1d, but the spot size becomes about four times lower due to the shorter wavelength. These together result in an ultrabright x-ray pulse with brilliance of about 7.5×10^{23} photons s^{-1} mm^{-2} $mrad^{-2}$ $0.1\%BW^{-1}$, which is much brighter than the record obtained in laser-based x-ray sources via the LWFA regime[14]. The reason for the higher critical energy can be attributed to the fact that the absolute values of the peak fields are twice larger than the case with wavelength of 800 nm, though their normalized value is the same. The stronger fields lead to stronger radiation. Note that the similarity theory is not applicable when the radiation reaction is considered.

Another feasible approach to further enhance the photon flux without consuming too many laser energies is using a laser pulse with an elliptical focal spot. An straightforward idea would be increasing the size of r_z which may further linearly enhance the number of accelerated electrons and also the photon flux. However, we found that increasing the size of r_y is a more efficient approach. For example, by increasing the size of r_y by 50% to 3.53 λ and remaining r_z and other parameters the same as the case with $n_e = 200n_c$ described above (leading to a laser power of 225TW), the obtained photon flux reaches about 1.3×10^7 photons eV^{-1} around 5 keV [red line in Fig. 4b], slightly stronger than the linear scaling and about 15% higher than the case of increasing r_z. Our analysis shows that the reasons can be attributed to that not only the local laser intensity felt by the electrons is slightly increased, but also the effects induced by the Rayleigh length can be mitigated. Moreover, with an appropriately longer pulse duration, more electron nanobunches are pulled out, accelerated forward and wiggled at the lateral surfaces, emitting more photons, see Supplementary Note IV and Fig. S5.

In summary, we have theoretically and numerically demonstrated an electron acceleration and radiation mechanism, where a femtosecond laser pulse is incident on a solid tape target. The underlying physics is identified, where electrons are accelerated efficiently by the longitudinal component of the SPW and emit photons continuously in the transverse self-generated quasistatic electric and magnetic fields. Our 3D simulations show that a high-flux high-brilliance x-ray source can be obtained with a tabletop 100 TW-class femtosecond laser. This would greatly advance the development of the laser-plasma based x-ray sources as a compact platform for radiography studies and ultrafast diagnostics.

Methods
PIC simulation
The 3D PIC simulations are conducted with the VLPL code[89]. Since the short wavelength radiation cannot be resolved by the simulation grid, in

VLPL, the radiation spectrum is calculated by assuming that an angular distribution is peaked in the direction of the electron momentum and can be approximated with the δ function and the frequency spectrum $S(\omega/\omega_c)$, where $S(x) = x \int_x^\infty K_{5/3}(\xi)d\xi$ and $\omega_c = (3/2)\gamma^2|F_\perp|$ is the critical frequency determined by the instant electron γ and transverse force acting on the electron[59,90]. The recoil force on the electron exerted by the emitted photon is included into the equations of the electron motion. This model has been benchmarked against experimental results[11,15,90].

A y-polarized Gaussian laser pulse is normally incident on an edge of a longitudinally orientated microtape [see Fig. 1a]. The pulse has a normalized intensity of $a_0 = 20$ ($I_0 = 8.65 \times 10^{20}$ W/cm^2), wavelength of $\lambda = 0.8\ \mu m$, duration of $\tau_L = 30$fs (FWHM), and transverse spot size of $d_L = 4.7\ \lambda$, leading to a power of about 150 TW. Such laser systems have been widely constructed around the world with a compact size of $\sim 10 m^2$[91,92]. A microtape target with relativistically overdense electron density $n_e = 50n_c$ is used to save computational resources. Here $n_c = m_e\omega_L^2/4\pi e^2$ is the critical density, where m_e and e are the electron mass and charge, respectively. The plasma tape has dimensions of $x \times y \times z = 140\lambda \times 1\lambda \times 24\ \lambda$ to ensure large numbers of betatron oscillations and adapt to the simulation domain of $42\lambda \times 24\lambda \times 24\ \lambda$. It is sampled by $2800 \times 960 \times 240$ cells with each cell containing 8 macroparticles. To account for possible finite contrast in experiment, we put some preplasmas around the tape with scale lengths that can be achieved in current experimental conditions[81]. The preplasma at the front has $1\ \lambda$ linear density ramp and that at lateral surfaces has $0.25\ \lambda$ linear ramp. A moving window is employed.

For the simulations in the discussions of scaling law and robustness, except the parameters specified in the text, the others remain unchanged. In the simulation with higher electron density of $n_e = 200n_c$, finer resolutions along x- and y-directions (i.e., $h_x = 0.01\lambda$, $h_y = 0.0125\ \lambda$) are considered while the resolution along z-direction remains the same to reduce the simulation size. Collisions are neglected since the collisional time[79] is orders of magnitude longer than the time scale of interest.

Data availability

The data that support the findings of this study are available from the corresponding authors upon request.

Code availability

The PIC code VLPL is available from A.P. on reasonable request.

References

1. Rousse, A., Rischel, C. & Gauthier, J.-C. Femtosecond X-ray crystallography. *Rev. Mod. Phys.* **73**, 17 (2001).
2. Corde, S. et al. Femtosecond x-rays from laser-plasma accelerators. *Rev. Mod. Phys.* **85**, 1 (2013).
3. Albert, F. & Thomas, A. G. R. Applications of laser wakefield accelerator-based light sources. *Plasma Phys. Control. Fusion* **58**, 103001 (2016).
4. See https://www.esrf.eu for information about European Synchrotron facility ESRF.
5. Raimondi, P. ESRF-EBS: The extremely brilliant source project. *Synchrotron Radiat. News.* **29**, 8 (2016).
6. See https://www.xfel.eu for information about the European XFEL facility.
7. Altarelli, M. The European x-ray free-electron laser: Toward an ultra-bright, high repetition-rate x-ray source. *High Power Laser Sci. Eng.* **3**, e18 (2015).
8. Huang, N., Deng, H., Liu, B., Wang, D. & Zhao, Z. Features and futures of X-ray free-electron lasers. *The Innovation* **2**, 100097 (2021).
9. Prat, E., Dijkstal, P., Ferrari, E. & Reiche, S. Demonstration of Large Bandwidth Hard X-Ray Free-Electron Laser Pulses at SwissFEL. *Phys. Rev. Lett.* **124**, 074801 (2020).
10. Kiselev, S., Pukhov, A. & Kostyukov, I. X-ray generation in strongly nonlinear plasma waves. *Phys. Rev. Lett.* **93**, 135004 (2004).
11. Rousse, A. et al. Production of a keV X-ray beam from synchrotron radiation in relativistic laser-plasma interaction. *Phys. Rev. Lett* **93**, 135005 (2004).
12. Kneip, S. et al. Bright spatially coherent synchrotron X-rays from a table-top source. *Nat. Phys.* **6**, 980 (2010).
13. Kaluza, M. C. et al. Measurement of Magnetic-Field Structures in a Laser-Wakefield Accelerator. *Phys. Rev. Lett* **105**, 115002 (2010).
14. Cipiccia, S. et al. Gamma-rays from harmonically resonant betatron oscillations in a plasma wake. *Nat. Phys.* **7**, 867 (2011).
15. Schnell, M. et al. Optical control of hard X-ray polarization by electron injection in a laser wakefield accelerator. *Nat. Commun.* **4**, 2421 (2013).
16. Chen, M. et al. Tunable synchrotron-like radiation from centimeter scale plasma channels. *Light Sci. Appl.* **5**, e16015 (2016).
17. Ferri, J. et al. High-Brilliance Betatron gamma-Ray Source Powered by Laser-Accelerated Electrons. *Phys. Rev. Lett.* **120**, 254802 (2018).
18. Andriyash, I. A. et al. An ultracompact X-ray source based on a laser-plasma undulator. *Nat. Commun.* **5**, 4736 (2014).
19. Zhu, X.-L. et al. Efficient generation of collimated multi-GeV gamma-rays along solid surfaces. *Optica* **10**, 118 (2023).
20. Lei, B., Wang, J., Kharin, V., Zepf, M. & Rykovanov, S. gamma-Ray Generation from Plasma Wakefield Resonant Wiggler. *Phys. Rev. Lett.* **120**, 134801 (2018).
21. Lei, B. et al. Flexible x-ray source with tunable polarization and orbital angular momentum from Hermite-Gaussian laser modes driven plasma channel wakefield. *Phys. Rev. Accel. Beams.* **22**, 071302 (2019).
22. Lv, Q. Z., Raicher, E., Keitel, C. H. & Hatsagortsyan, K. Z. High-brilliance ultranarrow-band x rays via electron radiation in colliding laser pulses. *Phys. Rev. Lett.* **128**, 024801 (2022).
23. Ta, Phuoc, K. et al. Demonstration of the ultrafast nature of laser produced betatron radiation. *Phys. Plasmas* **14**, 080701 (2007).
24. Chaulagain, U. et al. Eli gammatron beamline: A dawn of ultrafast hard x-ray science. *Photonics* **9**, 853 (2022).
25. Rakowski, R. et al. Transverse oscillating bubble enhanced laser-driven betatron X-ray radiation generation. *Sci. Rep.* **12**, 10855 (2022).
26. Götzfried, J. et al. Physics of high-charge electron beams in laser-plasma wakefields. *Phys. Rev. X* **10**, 041015 (2020).
27. Couperus, J. P. et al. Demonstration of a beam loaded nanocoulomb-class laser wakefield accelerator. *Nat. Commun.* **8**, 487 (2017).
28. Cole, J. M. et al. High-resolution CT of a mouse embryo using a compact laser-driven X-ray betatron source. *Proc. Natl. Acad. Sci.* **115**, 6335 (2018).
29. Mo, M. Z. et al. Measurements of ionization states in warm dense aluminum with betatron radiation. *Phys. Rev. E* **95**, 053208 (2017).
30. Šmíd, M. et al. Highly efficient angularly resolving x-ray spectrometer optimized for absorption measurements with collimated sources. *Rev. Sci. Instrum.* **88**, 063102 (2017).
31. Hollinger, R. et al. Efficient picosecond x-ray pulse generation from plasmas in the radiation dominated regime. *Optica* **4**, 001344 (2017).
32. Mahieu, B. et al. Probing warm dense matter using femtosecond X-ray absorption spectroscopy with a laser-produced betatron source. *Nat. Commun.* **9**, 3276 (2018).
33. Kettle, B. et al. Single-shot multi-keV X-ray absorption spectroscopy using an ultrashort laser-wakefield accelerator source. *Phys. Rev. Lett.* **123**, 254801 (2019).
34. Morace, A. et al. Development of x-ray radiography for high energy density physics. *Phys. Plasmas* **21**, 102712 (2014).
35. Robinson, A. P. L. et al. Theory of fast electron transport for fast ignition. *Nucl. Fusion* **54**, 054003 (2014).
36. Jarrott, L. C. et al. Visualizing fast electron energy transport into laser-compressed high-density fast-ignition targets. *Nat. Phys.* **12**, 499 (2016).

37. Mariscal, D. A. et al. A flexible proton beam imaging energy spectrometer (PROBIES) for high repetition rate or single-shot high energy density (HED) experiments (invited). *Rev. Sci. Instrum.* **94**, 023507 (2023).

38. Glenzer, S. H. & Redmer, R. X-ray Thomson scattering in high energy density plasmas. *Rev. Mod. Phys.* **81**, 1625 (2009).

39. Ping, Y. et al. Solid iron compressed up to 560 GPa. *Phys. Rev. Lett.* **111**, 065501 (2013).

40. Chin, D. A. et al. Emission phases of implosion sources for x-ray absorption fine structure spectroscopy. *Phys. Plasmas* **29**, 052702 (2022).

41. Döppner, T. et al. Observing the onset of pressure-driven K-shell delocalization. *Nature* **618**, 270 (2023).

42. Fourmaux, S., Hallin, E., Chaulagain, U., Weber, S. & Kieffer, J. Laser-based synchrotron X-ray radiation experimental scaling. *Opt. Express* **28**, 3147 (2020).

43. Lamac, M., Chaulagain, U., Jurkovic, M., Nejdl, J. & Bulanov, S. V. Two-color nonlinear resonances in betatron oscillations of laser accelerated relativistic electrons. *Phys. Rev. Research* **3**, 033088 (2021).

44. Kozlova, M. et al. Hard X rays from laser-wakefield accelerators in density tailored plasmas. *Phys. Rev. X* **10**, 011061 (2020).

45. Yu, C. et al. Enhanced betatron radiation by steering a laser-driven plasma wakefield with a tilted shock front. *Appl. Phys. Lett.* **112**, 133503 (2018).

46. Lobok, M. G., Andriyash, I. A., Vais, O. E., Malka, V. & Bychenkov, V. Y. Bright synchrotron radiation from relativistic self-trapping of a short laser pulse in near-critical density plasma. *Phys. Rev. E* **104**, L053201 (2021).

47. Fan, L. et al. Collimated gamma beams with high peak flux driven by laser-accelerated electrons. *High Power Laser Sci. Eng.* **11**, e26 (2023).

48. Rechatin, C. et al. Observation of Beam Loading in a Laser-Plasma Accelerator, "Observation of beam loading in a laser-plasma accelerator. *Phys. Rev. Lett.* **103**, 194804 (2009).

49. Pukhov, A., Sheng, Z.-M. & Meyer-ter-Vehn, J. Particle acceleration in relativistic laser channels. *Phys. Plasmas* **6**, 2847 (1999).

50. Robinson, A. P. L., Arefiev, A. V. & Neely, D. Generating "superponderomotive" electrons due to a non-wake-field interaction between a laser pulse and a longitudinal electric field. *Phys. Rev. Lett.* **111**, 065002 (2013).

51. Huang, T. W. et al. Nonlinear parametric resonance of relativistic electrons with a linearly polarized laser pulse in a plasma channel. *Phys. Plasmas* **24**, 043105 (2017).

52. Gong, Z., Hatsagortsyan, K. Z. & Keitel, C. H. Retrieving transient magnetic fields of ultrarelativistic laser plasma via ejected electron polarization. *Phys. Rev. Lett.* **127**, 165002 (2021).

53. Rosmej, O. N. et al. High-current laser-driven beams of relativistic electrons for high energy density research. *Plasma Phys. Control. Fusion* **62**, 115024 (2020).

54. Ma, Y.-Y. et al. Dense quasi-monoenergetic attosecond electron bunches from laser interaction with wire and slice targets. *Phys. Plasmas* **13**, 110702 (2006).

55. Wang, W.-M. et al. Collimated ultrabright gamma rays from electron wiggling along a petawatt laser-irradiated wire in the QED regime. *Proc. Nat. Acad. Sci.* **115**, 9911 (2018).

56. Shen, X. F., Pukhov, A., Günther, M. M. & Rosmej, O. N. Bright betatron x-rays generation from picosecond laser interactions with long-scale near critical density plasmas. *Appl. Phys. Lett.* **118**, 134102 (2021).

57. Shou, Y. et al. Brilliant femtosecond-laser-driven hard X-ray flashes from carbon nanotube plasma. *Nat. Photonics* **17**, 137 (2023).

58. Kneip, S. et al. Observation of synchrotron radiation from electrons accelerated in a petawatt-laser-generated plasma cavity. *Phys. Rev. Lett.* **100**, 105006 (2008).

59. Yu, T.-P., Pukhov, A., Sheng, Z.-M., Liu, F. and Shvets, G. Bright betatronlike x rays from radiation pressure acceleration of a mass-limited foil target. *Phys. Rev. Lett.* **110**, 045001 (2013).

60. Zhang, X., Khudik, V. N. & Shvets, G. Synergistic laser-wakefield and direct-laser acceleration in the plasma-bubble regime. *Phys. Rev. Lett.* **114**, 184801 (2015).

61. Huang, T. W. et al. Characteristics of betatron radiation from direct-laser-accelerated electrons. *Phys. Rev. E* **93**, 063203 (2016).

62. Shen, X. F., Pukhov, A., Qiao, B. Synergistic longitudinal acceleration and transverse oscillation in high-order harmonic generation. arXiv preprint arXiv:2009.12918, 2020.

63. Perevalov, S. E., Pukhov, A. M., Starodubtsev, M. V. & Soloviev, A. A. Laser peeler regime of high-harmonic generation for diagnostics of high-power focused laser pulses. *Matter Radiation at Extremes* **8**, 3 (2023).

64. Lamac, M., Mima, K., Nejdl, J., Chaulagain, U. & Bulanov, S. V. Anomalous relativistic emission from self-modulated plasma mirrors. *Phys. Rev. Lett.* **131**, 205001 (2023).

65. Yu, X. Q. et al. Megaelectronvolt electron acceleration driven by terahertz surface waves. *Nat. Photonics* **17**, 957 (2023).

66. Fedeli, L. et al. Electron acceleration by relativistic surface plasmons in laser-grating interaction. *Phys. Rev. Lett.* **116**, 015001 (2016).

67. Macchi, A. Surface plasmons in superintense laser-solid interactions. *Phys. Plasmas* **25**, 031906 (2018).

68. Shen, X. F., Pukhov, A. & Qiao, B. Monoenergetic high-energy ion source via femtosecond laser interacting with a microtape. *Phys. Rev. X* **11**, 041002 (2021).

69. Maier, S. A. et al. Theory of surface plasmons and surface-plasmon polaritons. *Rep. Prog. Phys.* **70**, 1 (2006).

70. Sarma, J., McIlvenny, A., Das, N., Borghesi, M. & Macchi, A. Surface plasmon-driven electron and proton acceleration without grating coupling. *New J. Phys.* **24**, 073023 (2022).

71. Wilks, S. C., Kruer, W. L., Tabak, M. & Langdon, A. B. Absorption of ultra-intense laser pulses. *Phys. Rev. Lett.* **69**, 1382 (1992).

72. Yi, L. Q., Pukhov, A., Thanh, P. L. & Shen, B. F. Bright X-ray source from a laser-driven microplasma waveguide. *Phys. Rev. Lett.* **116**, 115001 (2016).

73. Tan, J. H. et al. Observation of high efficiency Betatron radiation from femtosecond petawatt laser irradiated near critical plasmas, arXiv:2109.12467.

74. Tückmantel, T., Pukhov, A., Liljo, J. & Hochbruck, M. Three-dimensional relativistic particle-in-cell hybrid code based on an exponential integrator. *IEEE Trans. Plasma Sci.* **38**, 2383 (2010).

75. Martinez, B., d'Humiéres, E. & Gremillet, L. Synchrotron radiation from ultrahigh-intensity laser-plasma interactions and competition with Bremsstrahlung in thin foil targets. *Phys. Rev. Res.* **2**, 043341 (2020).

76. Crow, J. E., Auer, P. L. & Allen, J. E. The expansion of a plasma into a vacuum. *J. Plasma Phys.* **14**, 65 (1975).

77. Jackson, J. D. Classical Electrodynamics, 3rd ed. (Wiley, New York, 1998).

78. Gibbon, P. & Förster, E. Short-pulse laser-plasma interactions. *Plasma Phys. Control. Fusion* **38**, 769 (1996).

79. Gibbon, P. Short Pulse Laser Interaction with Matter, (Imperial College Press, London, 2005).

80. Xu, X. et al. Production of 100-TW single attosecond x-ray pulse. *Optica* **7**, 355 (2020).

81. Macchi, A., Borghesi, M. & Passoni, M. Ion acceleration by superintense laser-plasma interaction. *Rev. Mod. Phys.* **85**, 751 (2013).

82. Henig, A. et al. Radiation-Pressure Acceleration of Ion Beams Driven by Circularly Polarized Laser Pulses. *Phys. Rev. Lett.* **103**, 245003 (2009).

83. Alejo, A. et al. Stabilized Radiation Pressure Acceleration and Neutron Generation in Ultrathin Deuterated Foils. *Phys. Rev. Lett.* **129**, 114801 (2022).

84. Doumy, G. et al. Complete characterization of a plasma mirror for the production of high-contrast ultraintense laser pulses. *Phys. Rev. E* **69**, 026402 (2004).
85. Scott, G. G. et al. Optimization of plasma mirror reflectivity and optical quality using double laser pulses. *New J. Phys.* **17**, 033027 (2015).
86. Li, S. et al. A laser-plasma accelerator driven by two-color relativistic femtosecond laser pulses. *Sci. Adv.* **5**, eaav7940 (2019).
87. Wang, Y. et al. 0.85 PW laser operation at 3.3 Hz and high-contrast ultrahigh-intensity lambda = 400 nm second-harmonic beamline. *Opt. Lett.* **42**, 3828 (2017).
88. Hollinger, R. et al. Extreme ionization of heavy atoms in solid-density plasmas by relativistic second-harmonic laser pulses. *Nat. Photonics* **14**, 607 (2020).
89. Pukhov, A. Particle-In-Cell Codes for Plasma-based Particle Acceleration. *CERN Yellow Rep.* **1**, 181 (2016).
90. Williamson, B. et al. Betatron radiation diagnostics for AWAKE Run 2. *Nucl. Instrum. Methods Phys. Res. A* **971**, 164076 (2020).
91. Danson, C. et al. Petawatt and Exawatt Class Lasers Worldwide. *High Power Laser Sci. Eng.* **7**, e54 (2019).
92. https://www.thalesgroup.com/en

Author contributions
X.F.S. and A.P. conceived the scheme and X.F.S conducted the simulations and analyzed the results. X.F.S. wrote the manuscript with contributions from A.P. and B.Q.

Competing interests
The authors declare no competing interests.

Additional information
Supplementary information The online version contains supplementary material available at https://doi.org/10.1038/s42005-024-01575-z.

Correspondence and requests for materials should be addressed to Alexander Pukhov or Bin Qiao.

Peer review information *Communications Physics* thanks Zhengming Sheng and the other, anonymous, reviewer(s) for their contribution to the peer review of this work.

Reprints and permissions information is available at http://www.nature.com/reprints

Publisher's note Springer Nature remains neutral with regard to jurisdictional claims in published maps and institutional affiliations.